



## A new hematite formation mechanism for Mars

Michelle E. MINITTI,<sup>1\*</sup> Melissa D. LANE,<sup>2</sup> and Janice L. BISHOP<sup>3</sup>

<sup>1</sup>Center for Meteorite Studies, Arizona State University, Box 871404, Tempe, Arizona 85287–1404, USA

<sup>2</sup>Planetary Science Institute, 1700 E. Fort Lowell Road, Suite 106, Tucson, Arizona 85719, USA

<sup>3</sup>SETI Institute/NASA-ARC, 515 N. Whisman Road, Mountain View, California 94043, USA

\*Corresponding author. E-mail: [minitti@asu.edu](mailto:minitti@asu.edu)

(Received 9 June 2004; revision accepted 29 November 2004)

---

**Abstract**—The origin of hematite detected in Martian surface materials is commonly attributed to weathering processes or aqueous precipitation. Here, we present a new hematite formation mechanism that requires neither water nor weathering. Glass-rich basalts with Martian meteorite-like chemistry (high FeO, low Al<sub>2</sub>O<sub>3</sub>) oxidized at high (700 and 900 °C) temperatures in air and CO<sub>2</sub>, respectively, form thin (<1 μm) hematite coatings on their outermost surfaces. Hematite is manifested macroscopically by development of magnetism and a gray, metallic sheen on the glass surface and microscopically by Fe enrichment at the glass surface observed in element maps. Visible and near-infrared, thermal infrared, and Raman spectroscopy confirm that the Fe enrichment at the oxidized glass surfaces corresponds to hematite mineralization. Hematite formation on basaltic glass is enabled by a mechanism that induces migration of Fe<sup>2+</sup> to the surface of an oxidizing glass and subsequent oxidation to form hematite. A natural example of the hematite formation mechanism is provided by a Hawaiian basalt hosting a gray, metallic sheen that corresponds to a thin hematite coating. Hematite coating development on the Hawaiian basalt demonstrates that Martian meteorite-like FeO contents are not required for hematite coating formation on basalt glass and that such coatings form during initial extrusion of the glassy basalt flows. If gray hematite originating as coatings on glassy basalt flows is an important source of Martian hematite, which is feasible given the predominance of igneous features on Mars, then the requirement of water as an agent of hematite formation is eliminated.

---

### INTRODUCTION

Hematite is a known and important component of Martian surface mineralogy. The visible and near-infrared spectral character of Martian bright, dusty regions is explained by the presence of minor amounts of two forms of hematite. The featureless ferric absorption edge between 0.3–0.7 μm results from nanophase hematite and the weak absorption near 0.86 μm found in some regions on Mars requires subordinate amounts of fine-grained (~≤10 μm), yet crystalline, red hematite (Morris et al. 1989; Bell et al. 1990; Merenyi et al. 1996). In the thermal infrared, coarse gray hematite (Lane et al. 1999; Christensen et al. 2000b) was detected by the Mars Global Surveyor (MGS) Thermal Emission Spectrometer (TES) in three separate regions on Mars, always as a component of layered, presumably sedimentary, terranes (Christensen et al. 2000b, 2001b). Strong absorptions at 315, 461, and 560 cm<sup>-1</sup> observed by TES are characteristic of coarse, gray hematite (Christensen et al. 2000b, 2001b; Lane et al. 2002; Glotch et al. 2004).

The presence and physical character of hematite on Mars is used to assess conditions on the Martian surface responsible for hematite formation. The nanophase, red crystalline, and coarse gray forms of hematite observed on Mars are associated with a variety of different formation mechanisms. Processes involving the alteration and weathering of basaltic materials are the preferred formation mechanisms of the hematite phases present in the bright region dust. One example of such a process is palagonitization of basaltic glass (Morris et al. 1990, 1993, 2000), which can yield both nanophase (amorphous) and fine-grained (crystalline) red hematite. In addition to palagonitic alteration, pedogenic and solfataric alteration of basaltic glasses are all capable of producing nanophase and/or fine-grained red hematite (e.g., Bishop et al. 1998, 2002, 2004; Morris et al. 1990, 1993, 2000; Schiffman et al. 2000, 2002). The preferred formation mechanism proposed by Christensen et al. (2000) for the coarse, gray hematite is precipitation from Fe-rich water (at ambient or hydrothermal temperatures). Glotch et al. (2004), however, argue that the TES-observed hematite signature is

better explained by hematite resulting from the low-temperature ( $\sim 300$  °C) transformation of goethite. Glotch et al. suggest that the goethite precursor could result from precipitation in water or from aqueous alteration. An alternative explanation for the gray hematite is that it is present as a thin coating (Kirkland et al. 2004), but Kirkland et al. do not discuss or propose a formation mechanism for such coatings. The involvement of water in the formation of the gray hematite appears to be supported by the Mars Exploration Rover (MER) Opportunity observations that indicate the presence of sulfates and hematite concretions (Christensen et al. 2004) in an outcrop containing bedforms originating in flowing water (Herkenhoff et al. 2004).

A previously undescribed hematite formation mechanism for Mars was suggested by a recent study of the effects of crystallinity and oxidation on the spectra of Martian basalts (Minitti et al. 2002). Minitti et al. (2002) oxidized Martian basaltic samples with a range of glass contents (crystallinities) in air at 700 °C. For glass-rich samples, oxidation yielded samples with visible, near-infrared, and thermal infrared spectra consistent with the presence of hematite. The hematite signature appeared to originate from a thin, metallic sheen developed over glassy surfaces. However, Minitti et al. did not confirm the presence of hematite with other analyses. The apparent presence of a uniform hematite coating on the surfaces of oxidized glasses suggested that hematite could form via oxidation during extrusion of glass-bearing basaltic flows. In this study, we confirm that oxidation of basalt glass leads to the formation of a thin, uniform hematite coating and refine the conditions under which glass oxidation results in hematite formation with both natural and additional laboratory samples. The glass oxidation mechanism of hematite formation acts in a strictly igneous environment and may provide an important source of hematite given the widespread occurrence of igneous materials observed on Mars. The mechanism, which requires neither chemical weathering nor water, has implications for the role and importance of water in the formation of hematite present in Martian surface materials.

## EXPERIMENTAL TECHNIQUES

To confirm the formation of a uniform hematite coating on oxidized basaltic glass, we used basaltic glass samples synthesized by Minitti et al. (2002). The samples included glass-rich (85% glass + 15% pigeonite phenocrysts) and fully glassy basalts with Martian meteorite-like compositions (i.e., high FeO, low  $\text{Al}_2\text{O}_3$ ) (Minitti and Rutherford 2000). Minitti et al. (2002) ground and sieved the glass-rich sample to a 75–500  $\mu\text{m}$  particle size and the purely glassy sample to a  $<75$   $\mu\text{m}$  particle size. The samples were subjected to oxidation under different conditions. Minitti et al. (2002) held the glass-rich sample at 700 °C in air for 7 days. For this study, we initially held the fully glassy sample at 350 °C in air for 14 days and,

in a separate experiment, held the same sample at 900 °C in  $\text{CO}_2$  for 3 days. We used the pure glass sample in the latter  $\text{CO}_2$  experiment only after determining that the 350 °C experiment had no effect on the chemistry of the sample (see Results section). The 350 °C experiment was intended to explore the effects of oxidation at low temperatures and the  $\text{CO}_2$ -based experiment was conducted in an effort to mimic oxidation in the Martian atmosphere. Despite using pure  $\text{CO}_2$ , oxygen was available in the environment around the sample due to the reaction  $\text{CO}_2 \rightarrow \text{CO} + \frac{1}{2}\text{O}_2$ . At the temperature of the experiment,  $\log f_{\text{O}_2}$  of the environment was  $\sim 10^{-8}$  (Deines et al. 1974), corresponding to an oxygen fugacity near the hematite-magnetite buffer.

## ANALYTICAL TECHNIQUES

We assessed the chemistry and distribution of elements in the samples using the JEOL 845 scanning electron microscope (SEM) at Arizona State University (ASU). Thin sections of the oxidized glasses were studied via backscattered electron (BSE) imaging and X-ray mapping. Images and maps were made with a focused, 15 kV, 0.6–2 nA beam.

Raman spectroscopy was employed to investigate the mineralogical nature of the oxidized basalt glasses. We collected Raman spectra in the Mineral Spectroscopy Laboratory at the California Institute of Technology using a Renishaw M1000 Micro Raman spectrometer with a 514.5 nm argon laser operated at 0.5 mW. A double-wedged quartz depolarizer was used to minimize or eliminate polarization effects in the Raman spectra. The laser was focused onto the sample through either 20 $\times$  or 50 $\times$  objective lenses producing 5–8  $\mu\text{m}$  or 3–5  $\mu\text{m}$  spots, respectively. Collection times varied between 10–240 sec. We also collected Raman spectra at Arizona State University using a Jobin-Yvon Triax 550 spectrometer coupled with a Spectra Physics 2020-5 argon laser. Raman spectra were excited with the 514.5 nm line of the laser that delivered  $\sim 10$  mW of power to the sample surface through a 50 $\times$  objective lens. We defocused the laser beam on the sample to a spot size of  $\sim 4$ –6  $\mu\text{m}$  and collected spectra over three 240-sec intervals. Data from each interval were added together to produce a final spectrum. We used combinations of collection time, spot size, and laser power to prevent degradation or alteration of the analyzed samples under the laser spot. We selected analysis conditions guided by the studies of de Faria et al. (1997) and Shebanova and Lazor (2003), which focused on constraining proper analysis conditions for Fe oxides and oxyhydroxides. During the ASU Raman analyses, we monitored the spectra after each collection interval to ensure no beam-induced change appeared in the spectra and after both the ASU and Caltech analyses, the analyzed samples were examined under reflected light to confirm the absence of laser-induced damage. Samples of pure phases, including hematite,

maghemite, magnetite, goethite, lepidocrocite, augite, enstatite, and unoxidized basalt glass, were analyzed to obtain Raman spectra for comparison to the experimental samples. Some of the pure phase spectra were collected at ASU or Caltech under the same conditions as the experimental samples and the remaining spectra were collected at Caltech using a red, 780 nm diode laser delivering 0.5 mW to the samples through a 50× objective. Collection times for the spectra obtained with the 780 nm laser lasted 60 sec.

Characterization of the reflectance and emission spectra of the basalt glasses was carried out in order to compare the sample spectra to the remotely sensed spectra of Mars. Visible and near-infrared (VNIR) and mid-infrared spectra were acquired from the unoxidized samples by Minitti et al. (2002) using the Keck/NASA RELAB facility at Brown University. VNIR spectra between 0.32–2.55  $\mu\text{m}$  at a 0.01  $\mu\text{m}$  sampling interval were collected using the bidirectional spectrometer with an incidence angle of 30° and an emergence angle of 0° (Minitti et al. 2002). Mid-infrared spectra were collected using an on-axis, biconical FTIR spectrometer from ~400–5500  $\text{cm}^{-1}$  at 4  $\text{cm}^{-1}$  intervals with 30° incidence and 30° emergence angles (Minitti et al. 2002). The mid-infrared reflectance spectra of the unoxidized samples were converted to emissivity using Kirchoff's law ( $e = 1 - r$ ). We collected VNIR spectra of the oxidized samples at the RELAB facility under the same conditions used by Minitti et al. (2002). We also obtained thermal infrared spectra of the oxidized samples between 200–2000  $\text{cm}^{-1}$  with 2  $\text{cm}^{-1}$  spectral resolution at the Arizona State University Thermal Emission Spectroscopy Laboratory. Each analysis involved 320 scans by the spectrometer to produce an individual spectrum. Multiple spectra of each sample were obtained and averaged together to produce a final spectrum with improved signal-to-noise. The thermal infrared spectral data were also resampled to 10  $\text{cm}^{-1}$  spectral resolution for comparison to MGS TES data (Christensen et al. 1992, 2001a).

## RESULTS

### Sample Description

Oxidation in the high-temperature experiments caused significant transformation of the samples. Internally, the glasses are partially devitrified into nm-size pyroxene crystallites (Minitti et al. 2002) or  $\mu\text{m}$ -size dendrites. The crystallites formed in the glass oxidized at 700 °C, whereas the dendrites formed in the glass oxidized at 900 °C. Formation of the larger dendrites in the 900 °C experiment is likely due to the higher experiment temperature leading to coarser devitrification products in the glass. Oxidation also caused both high-temperature oxidation products to become magnetic despite the lack of formation of Fe-Ti oxide phenocrysts during the original basalt synthesis experiments. Externally, the black, vitreous luster of the glasses altered to a

gray, metallic sheen that can be removed with gentle abrasion. Thus, oxidation created a coating on the glassy surfaces of the basalts oxidized at high temperature. The low-temperature oxidation experiment product did not develop devitrification products, a coating or magnetism, which indicated that the low-temperature experiment did not significantly alter the starting material.

### SEM Analyses

SEM analyses revealed the chemistry and elemental distributions of the oxidation-induced coatings on the samples. X-ray maps indicated that the samples oxidized both in air and in  $\text{CO}_2$  at high temperature exhibit layers of Fe and Ca enrichment at the surfaces of the glasses (Figs. 1a and 1b). The Fe-rich layer is always exterior to the Ca-rich layer. The thicknesses of Fe- and Ca-rich layers on the air-oxidized sample range from 1–1.5  $\mu\text{m}$  and the thicknesses of layers on the  $\text{CO}_2$ -oxidized sample range from 0.2–0.7  $\mu\text{m}$ . The Fe-rich layers appear to correspond to bright rims visible in the BSE images of the samples (Figs. 1c and 1d). The  $\text{CO}_2$ -oxidized sample also has a zone of moderate (relative to the outermost Fe layer) Fe enrichment interior to the Fe- and Ca-rich layers. The element distributions in this zone resemble those observed in pyroxene clusters formed by devitrification of the glass. Thus, the moderately Fe-enriched zone is interpreted as pyroxene developed as a near-surface devitrification product. The exact chemical classification of the pyroxene devitrification products was not determined with the SEM data. In contrast to the high-temperature oxidation products, no chemical gradient was developed during the 350 °C oxidation experiment (Fig. 1e). We interpret the lack of chemical gradient development as further evidence (in addition to no devitrification product, coating, or magnetism development) that the low-temperature oxidation step did not meaningfully affect the pure glass sample and that the sample could be used in the 900 °C  $\text{CO}_2$  oxidation experiment.

### Raman Analyses

Chemistry alone does not reveal which Fe-rich and Ca-rich phases make up the coatings on the surfaces of the oxidized glasses. Raman analyses were used to determine the mineralogical nature of the Fe-rich and Ca-rich materials. Raman spectra of the air-oxidized samples obtained from both laboratories exhibit peaks near 221, 241, 291, 322, 407, and 610  $\text{cm}^{-1}$  and broad peaks near 480, 690, and 1311  $\text{cm}^{-1}$  (Fig. 2a). Similarly, Raman spectra of the  $\text{CO}_2$ -oxidized samples exhibit peaks near 223, 240, 290, 405, 491, 604, and 1310  $\text{cm}^{-1}$  and a broad peak near 664  $\text{cm}^{-1}$  (Fig. 2b). The relative sizes of the peaks vary between the ASU- and Caltech-collected spectra from both the air- and  $\text{CO}_2$ -oxidized samples. However, the consistent appearance of features in both the ASU and Caltech spectra strongly suggest that none

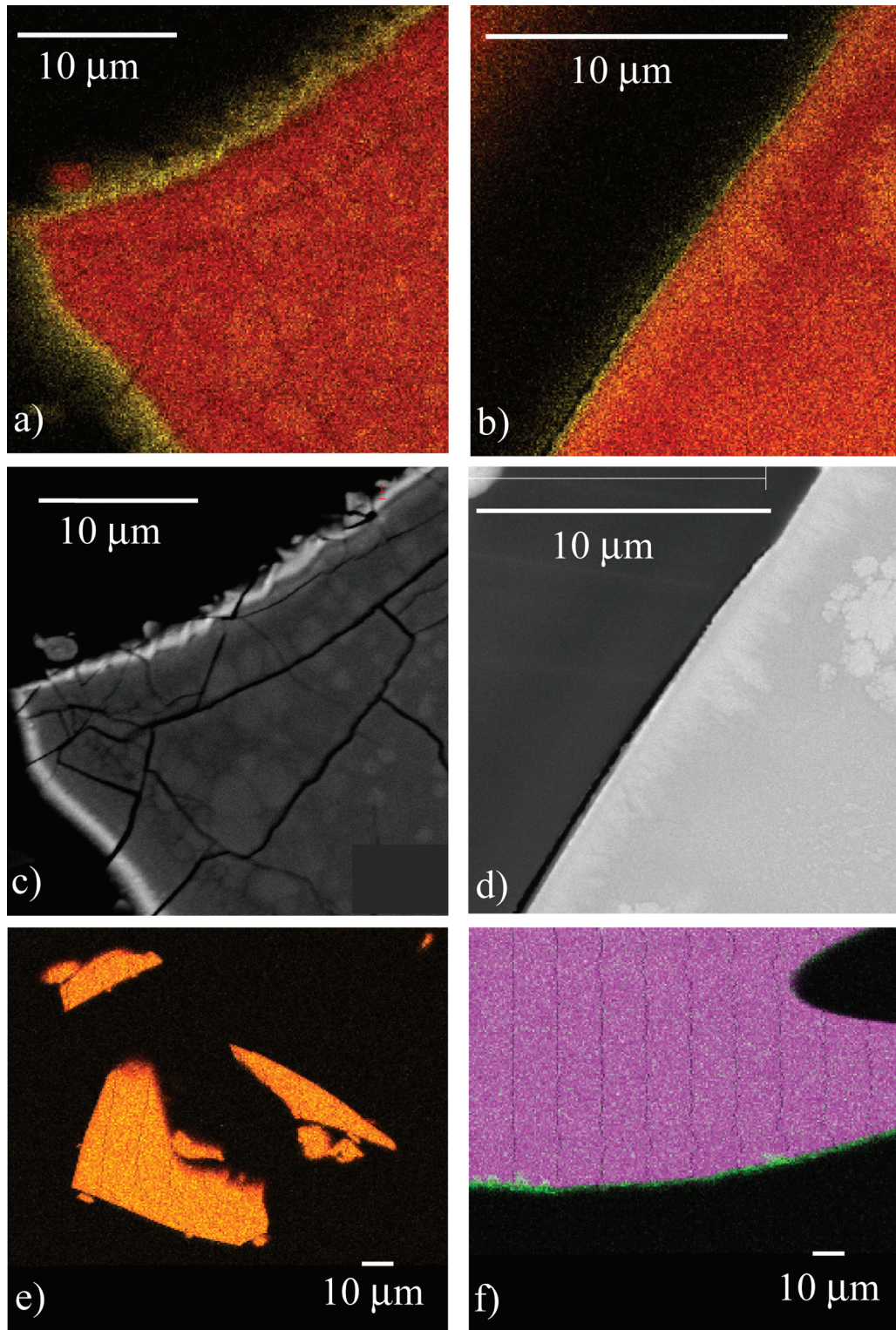


Fig. 1. SEM images of oxidized sample cross sections: a) X-ray element map of air-oxidized sample. Red corresponds to Si, yellow corresponds to Fe; b) X-ray element map of  $\text{CO}_2$ -oxidized sample. Red corresponds to Si, yellow corresponds to Fe; c) BSE image of air-oxidized sample. Bright rim at surface of sample corresponds to zone of Fe enrichment in (a); d) BSE image of  $\text{CO}_2$ -oxidized sample. Bright rim at surface of sample corresponds to zone of Fe enrichment in (b); e) X-ray element map of 350 °C, air-oxidized sample. Red corresponds to Si, yellow corresponds to Fe. Note the lack of Fe-enriched zone at the surfaces of the sample; f) X-ray elemental map of a cross section of a Hawaiian basalt exhibiting a gray, metallic sheen. Purple corresponds to Si, green corresponds to Fe. The Hawaiian basalt exhibits the same Fe enrichment at its surface as the experimentally-oxidized samples.

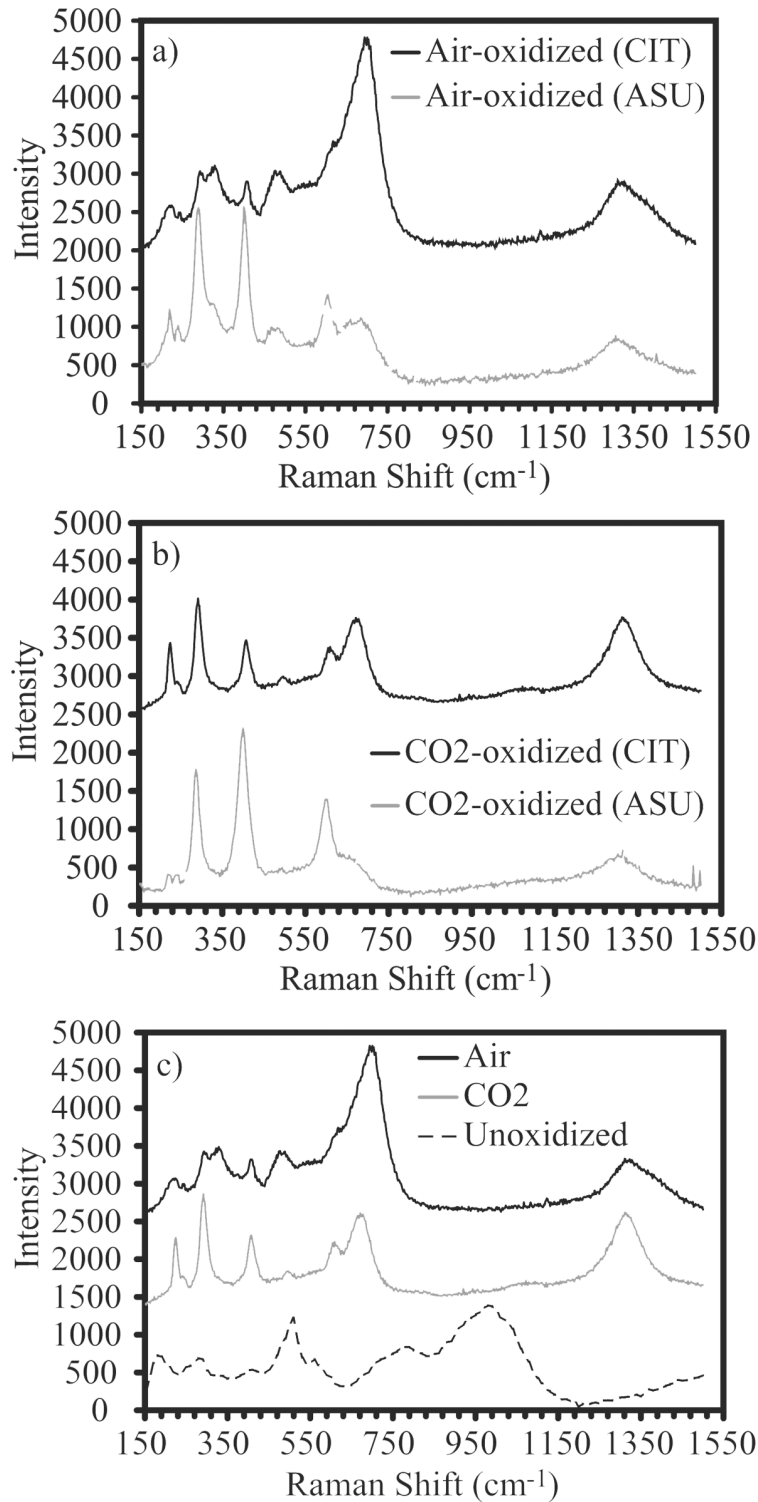


Fig. 2. a) Spectra from surfaces of air-oxidized samples collected at Caltech (black) and ASU (gray). The spectra are offset along the intensity axis for clarity; b) spectra from surfaces of CO<sub>2</sub>-oxidized samples collected at Caltech (black) and ASU (gray). The spectra are offset along the intensity axis for clarity; c) Raman spectra collected at Caltech from surfaces of air-oxidized (black) and CO<sub>2</sub>-oxidized (gray) samples and an unoxidized glass (dashed). The spectra are offset along the intensity axis for clarity. The differences between the oxidized sample spectra and the unoxidized glass spectrum in (c) indicate the occurrence of mineralization at the surfaces of the oxidized samples. The similarities between the spectra in (a) and between the spectra in (b) indicate that both sets of analyses detected the same mineralization. All spectra were excited using a 514.5 nm Ar laser.

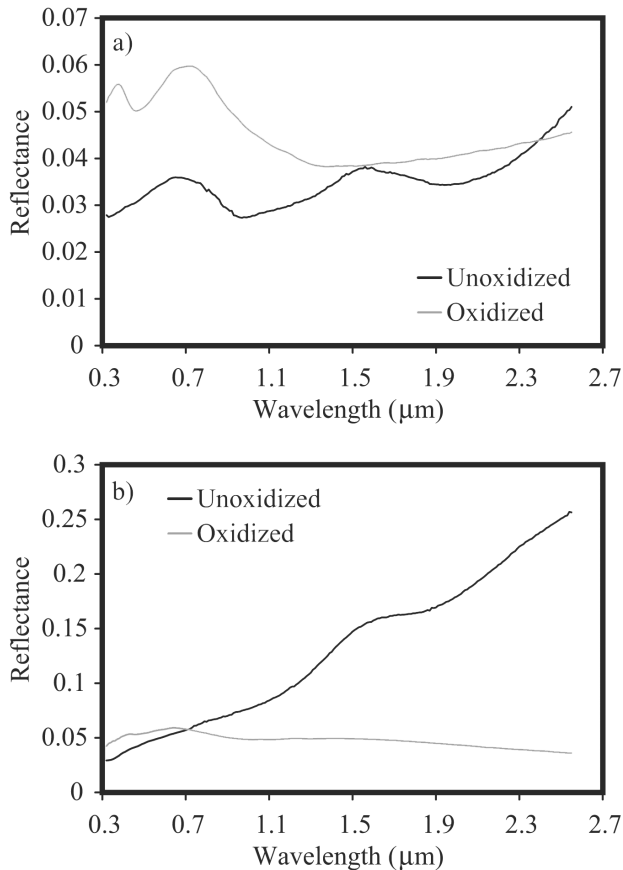


Fig. 3. Visible and near-infrared reflectance spectra of basalt glasses before (black) and after (gray) oxidation. The differences in brightness between the two pre-oxidation spectra arise from differences in particle sizes of the particulate samples; a) air-oxidized sample spectra. The oxidized spectrum is offset +0.02 along the reflectance axis for clarity; b) CO<sub>2</sub>-oxidized sample spectra.

of the features is due to analytical conditions. Each coating spectrum differs from the spectrum exhibited by an unoxidized, glassy Hawaiian basalt with broad peaks near 182, 275, 404, 505, 558, 778, and 980 cm<sup>-1</sup> (Fig. 2c). The Raman peaks exhibited by the coated surfaces of the experimentally oxidized basalt indicate that the coatings represent mineralization on the oxidized surface of the basalts.

### Visible and Infrared Spectroscopy

Spectral characterization of the coatings on the oxidized basalt glasses is important for phase identification and comparison to the spectra of Mars obtained via remote sensing. Comparison of the VNIR spectra of both the air- and CO<sub>2</sub>-oxidized samples before and after oxidation reveals the significant change in spectral character caused by oxidation (Fig. 3). Prior to oxidation, the basalt spectra have positive slopes and weak, broad absorptions near 1.1 and 1.9 μm, consistent with the glassy nature of the basalts. The spectrum of the air-oxidized basalt has an absorption at

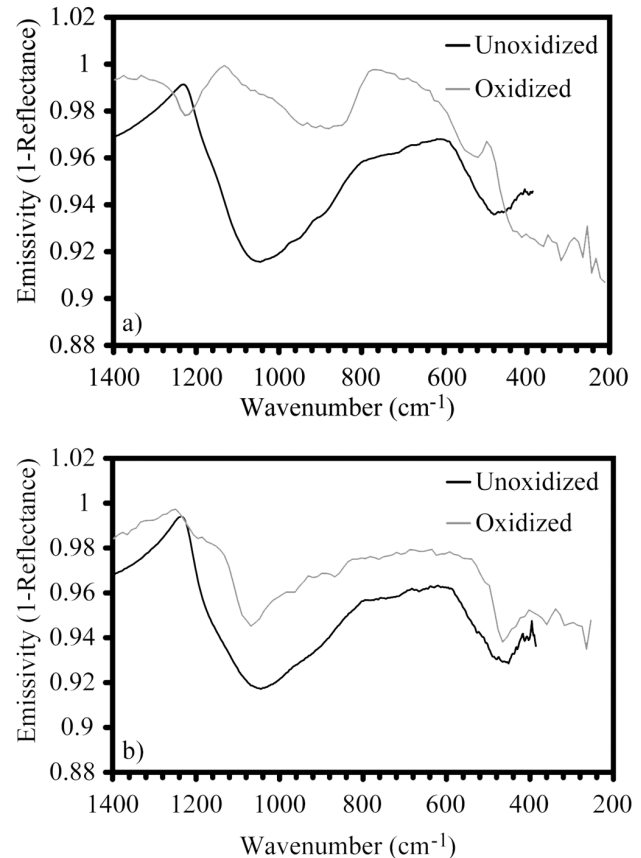


Fig. 4. Reflectance spectra (converted to emissivity) of the basalt glasses before oxidation (black) and emission spectra of basalt glasses after oxidation (gray). The lower wave number limits of the unoxidized spectra (~400 cm<sup>-1</sup>) represent the lower wave number limit of the collection technique at the time of measurement. The unoxidized spectra have spectral resolution of 2 cm<sup>-1</sup> and oxidized spectra have spectral resolution of 10 cm<sup>-1</sup>; a) air-oxidized sample spectra; b) CO<sub>2</sub>-oxidized sample spectra.

0.47 μm, a negative slope from ~0.74 to ~1.4 μm, and a positive slope at wavelengths longer than ~1.4 μm (Fig. 3a). The CO<sub>2</sub>-oxidized sample spectrum also has an absorption at 0.47 μm, but has an overall negative slope at wavelengths longer than 0.65 μm and an absorption near 1 μm (Fig. 3b). The absorption near 1 μm in the CO<sub>2</sub>-oxidized basalt spectrum most likely arises from the pyroxene devitrification products near the surface of the CO<sub>2</sub>-oxidized basalt.

Oxidation also induced changes to the emissivity spectra of the basalts. Before oxidation, both basalt spectra exhibit broad, featureless bands between 800–1200 cm<sup>-1</sup> and 400–600 cm<sup>-1</sup>, diagnostic of the amorphous nature of glass that dominates the modes of the samples (Fig. 4) (Simon and McMahon 1953). The glass-rich sample spectrum (before oxidation in air) has minor pyroxene absorptions between 800–1000 cm<sup>-1</sup> due to the pigeonite phenocrysts in the sample (Fig. 4a). After oxidation, the spectrum of the air-oxidized sample displays absorptions near 1230 cm<sup>-1</sup> and

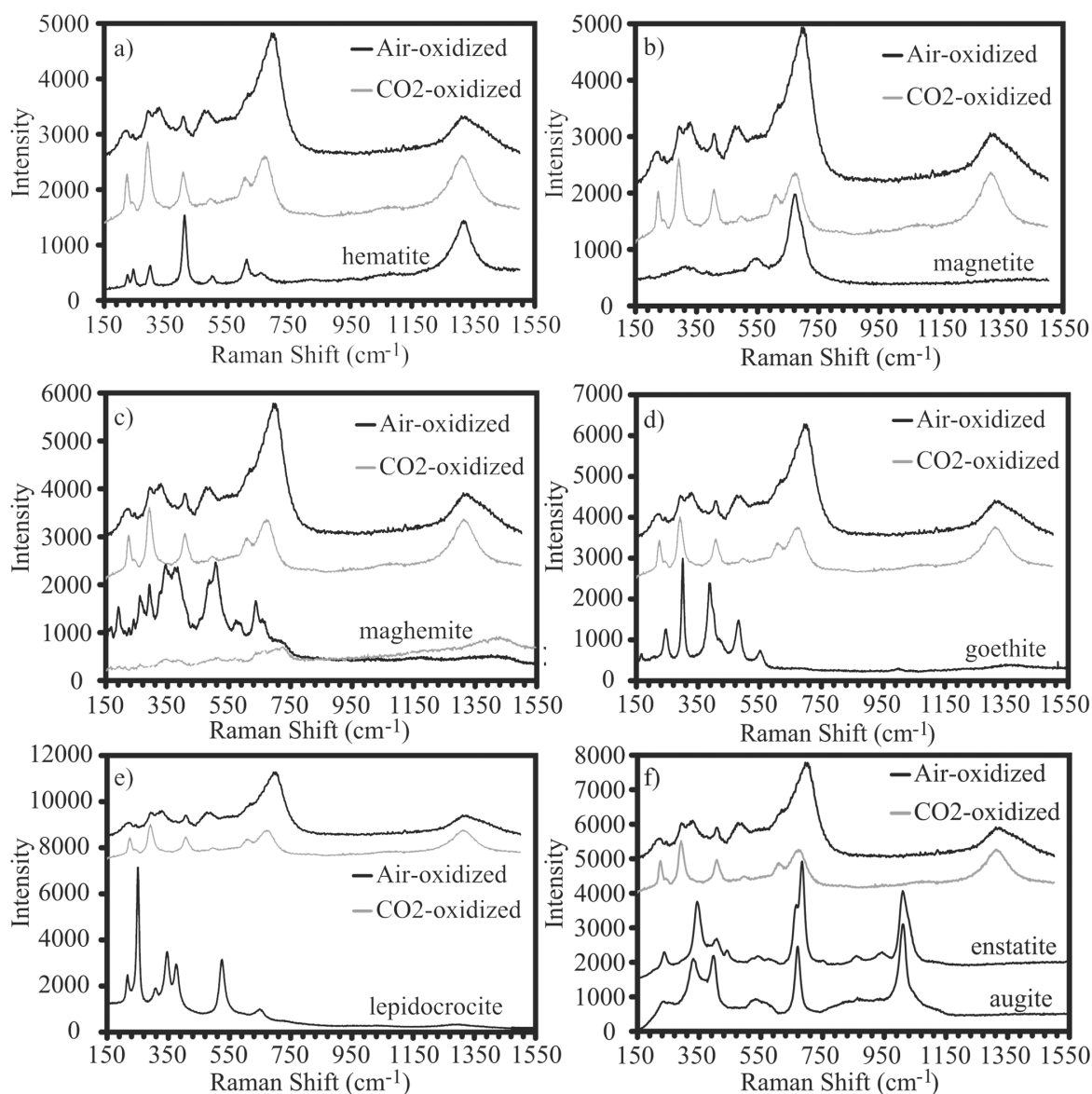


Fig. 5. Raman spectra from surfaces of air-oxidized (black) and CO<sub>2</sub>-oxidized (gray) samples compared to Raman spectra of a variety of iron oxides, iron oxyhydroxides, and pyroxenes. The spectra are offset along the intensity axis for clarity. All spectra, with the exception of one in (c), were collected at Caltech. The air-oxidized, CO<sub>2</sub>-oxidized, and hematite spectra were excited using a 514.5 nm Ar laser. The remaining mineral spectra in (b–f) were excited using a 780 nm diode laser; a) hematite comparison; b) magnetite comparison; c) maghemite comparison. The gray spectrum was collected at ASU; d) goethite comparison; e) lepidocrocite comparison; f) augite and enstatite pyroxene comparison. The strong similarities in peak positions between the oxidized sample and hematite spectra in (a) suggest that Fe enrichment at the surfaces of the oxidized samples corresponds to hematite.

540 cm<sup>-1</sup> and a narrowed broad feature between 800–1100 cm<sup>-1</sup>. The spectrum also exhibits a nearly flat, reduced-emissivity section between 200–400 cm<sup>-1</sup>, but it is not possible to assess the degree to which oxidation is responsible for the character of the spectrum between 200–400 cm<sup>-1</sup> given the lack of data for the unoxidized sample over this spectral range (Fig. 4a). In the spectrum of the CO<sub>2</sub>-oxidized sample, oxidation transforms the broad features of the unoxidized spectrum to narrower, V-shaped absorptions near 1070 and 466 cm<sup>-1</sup> (Fig. 4b). Oxidation also introduces minor

features into the spectrum of the CO<sub>2</sub>-oxidized sample near 1200 cm<sup>-1</sup> and between 800–1000 cm<sup>-1</sup>.

## DISCUSSION

### Interpretation of the Raman Data

Comparison of the Raman peak positions obtained from the oxidized basalt coatings to those obtained from known minerals facilitated identification of the phases in the coatings

(Fig. 5). In the air-oxidized Raman spectrum, peaks near 221, 241, 291, 407, 480, 610, 690, and 1311  $\text{cm}^{-1}$  correspond to peaks exhibited by gray hematite analyzed under the same conditions as the experimental samples (Fig. 5a). A better match to the hematite spectrum is made with the  $\text{CO}_2$ -oxidized sample spectrum. Each of the features in the  $\text{CO}_2$ -oxidized spectrum is accounted for by features in the gray hematite spectrum (Fig. 5a). Comparison of the oxidized basalt spectra and the spectra of other Fe oxides, Fe oxyhydroxides, and pyroxenes (Figs. 5b–5f) reveals that no other phase provides as consistent a match over all of the peak positions to the Raman spectra of the oxidized glasses as hematite does (Fig. 5a). The peak near 670  $\text{cm}^{-1}$  in the magnetite spectrum, however, could account for the relative size of the 690  $\text{cm}^{-1}$  and 664  $\text{cm}^{-1}$  peaks in the air-oxidized and  $\text{CO}_2$ -oxidized spectra, respectively. This observation suggests that some fraction of the Fe enrichment on the oxidized glass surfaces is due to the presence of magnetite. It is unclear to what degree magnetite and hematite contribute to the 690/664  $\text{cm}^{-1}$  peaks in the Raman spectra of the oxidized glasses, particularly given the factors that can affect relative peak positions, heights, and breadths (see below).

The relative peak positions, peak heights, and peak breadths differ among the spectra of the air-oxidized sample, the  $\text{CO}_2$ -oxidized sample and hematite (Fig. 5a). The peaks exhibited by the experimentally oxidized sample spectra are consistently offset to lower wave numbers relative to the peaks in the hematite spectrum, whereas peak positions among the experimental sample spectra are similar. Relative to the hematite spectrum, the experimentally oxidized sample spectra consistently tend to exhibit stronger peaks near 220, 290, and, in the Caltech-collected spectra, near 690  $\text{cm}^{-1}$  (664  $\text{cm}^{-1}$  for the  $\text{CO}_2$ -oxidized sample). The relative peak heights of experimentally oxidized sample spectra differ slightly from one another, primarily in the relative size of the broad peaks near 480 and 690  $\text{cm}^{-1}$  (664  $\text{cm}^{-1}$ ). Peak breadth variations are most pronounced between the peaks in the air-oxidized sample spectrum and those in the hematite spectrum. Peaks exhibited by the  $\text{CO}_2$ -oxidized sample spectrum are narrow relative to those of the air-oxidized sample spectrum.

The observed variations in peak position, height, and breadth can be explained by minor differences in the chemistry, crystallinity (point or line defects) or grain size of the hematite in the individual samples (e.g., Tuinstra and Koenig 1970; McMillan and Hofmeister 1988; Wang et al. 1998). The ability of minor crystal-chemical differences to influence the expression of peaks in the Raman spectrum of a single mineral is demonstrated by the multiple hematite Raman spectra in Fig. 6. The hematite spectra, obtained from a variety of forms of hematite, exhibit differences in peak occurrence, position, breadth, and relative height. The literature also corroborates the abilities of chemistry, crystallinity, and grain size to influence the expression of

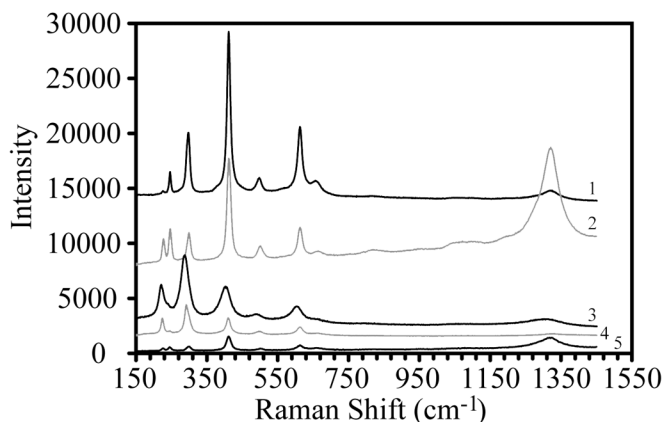


Fig. 6. Raman spectra of a variety of hematite samples illustrating the degree to which peak occurrence, position, breadth, and relative height can differ between samples of a single mineral. The spectra are offset along the intensity axis for clarity. All spectra were collected at Caltech. Spectra 1–4 were excited using a 780-nm diode laser; spectrum 5 was excited using a 514.5-nm Ar laser; 1) single crystal hematite; 2) hematite of unknown origin. Spectrum from the Caltech Raman database; 3) synthetic hematite powder; 4) hematite of unknown origin. Spectrum from the Caltech Raman database; 5) <500  $\mu\text{m}$  fraction of gray hematite from Republic, Michigan (sample courtesy of T. Glotch). The spectrum of this sample is also featured in Fig. 5a.

Raman peaks in a mineral spectrum. Any of these variables alone or in combination can affect relative peak positions (Wang et al. 1998), suggesting that hematite in the oxidized glass coatings has minor chemical impurities, structural defects, and/or small grain size relative to the analyzed hematite sample. Similarities of peak positions among the experimentally oxidized sample spectra suggest that the glass oxidation process produces hematite that has consistent chemistry and morphology. Deviations from nominal hematite chemistry and stoichiometry (presence of point defects) can also cause changes in relative peak heights (e.g., Tuinstra and Koenig 1970; McMillan and Hofmeister 1988), as can differences between the crystal orientations of the hematite in the coatings relative to the analyzed hematite. Similarities in peak heights among the air- and  $\text{CO}_2$ -oxidized sample spectra again suggest that the chemistry and morphology of hematite created in the oxidation process are internally consistent, but different from the analyzed hematite sample. Peak broadening can be attributed to lower degrees of crystallinity (e.g., Tuinstra and Koenig 1970). The narrower peaks exhibited by the  $\text{CO}_2$ -oxidized sample spectrum relative to the air-oxidized sample spectrum suggest that the hematite coating of the former sample is better crystallized than that of the latter. The higher degree of crystallinity of the hematite created in the  $\text{CO}_2$  oxidation is likely due to the higher temperature of the experiment rather than the oxidation environment, as higher temperatures permit a faster approach to equilibrium. In general, the specific positions and morphologies of the

Raman peaks in the oxidized sample spectra indicate that hematite of varying purity, crystallinity, or grain size is present in the coatings.

The minor feature at  $325\text{ cm}^{-1}$  in the air-oxidized sample spectrum appears in neither the hematite nor the  $\text{CO}_2$ -oxidized glass spectra (Fig. 5). A potential source of the  $325\text{ cm}^{-1}$  feature is pyroxene, either from the pigeonite phenocrysts formed during crystallization of the sample or from the nm-sized pyroxenes formed by devitrification of the glass during oxidation. Both orthopyroxenes and clinopyroxene exhibit a feature near  $330\text{ cm}^{-1}$  (Fig. 5f). Pyroxenes are also consistent with the broad features in the air-oxidized glass spectrum near  $690\text{ cm}^{-1}$  and in the  $\text{CO}_2$ -oxidized glass spectrum near  $664\text{ cm}^{-1}$ . A contribution from pyroxene to the  $690/664\text{ cm}^{-1}$  features could lessen the need to appeal to magnetite to explain the relative size of the  $690/664\text{ cm}^{-1}$  features. However, pyroxene devitrification products are present in and nearer to the surface of the  $\text{CO}_2$ -oxidized sample, yet its Raman spectrum does not contain the  $325\text{ cm}^{-1}$  feature. Further, neither the air-oxidized nor  $\text{CO}_2$ -oxidized sample spectra contain evidence of the large pyroxene feature near  $1010\text{ cm}^{-1}$  (Fig. 5f), which might be expected given the possible expression of the other major pyroxene peaks.

Another possible source of the  $325\text{ cm}^{-1}$  feature is the Ca-rich phase present interior to the hematite.  $\text{CaO}$  or  $\text{Ca}(\text{OH})_2$ , Ca-rich phases observed as glass oxidation products in earlier studies (e.g., Cooper et al. 1996; see also Hematite Formation Mechanism section below) are candidates to explain the Ca-rich layer below the hematite layer, but pure, stoichiometric  $\text{CaO}$  does not have a Raman active mode (G. Wolf, personal communication). If  $\text{Ca}(\text{OH})_2$  is the source of the Ca enrichment, the dominance of hematite-related peaks in the Raman spectrum suggests that it is only weakly Raman active. However, if  $\text{Ca}(\text{OH})_2$  were responsible for the  $325\text{ cm}^{-1}$  feature, the feature would be expected to appear in the spectrum of the  $\text{CO}_2$ -oxidized sample because it also has a Ca-rich layer interior to the hematite layer.

The third possibility is that the  $325\text{ cm}^{-1}$  feature is due to differences in the nature of the glasses in the air- and  $\text{CO}_2$ -oxidized samples. Glasses have the potential to exhibit a variety of features (e.g., Fig. 2). It is possible that the air-oxidized glass has a unique Raman signature due to alteration of the glass through formation of the finely distributed, nm-sized pyroxenes and that it differs from the signature of the glass surrounding the larger-scale pyroxene clusters in the  $\text{CO}_2$ -oxidized glass. The presence of this feature in the air-oxidized spectrum and its absence in  $\text{CO}_2$ -oxidized spectrum does not alter the conclusion that hematite is present at the surface of the oxidized glasses.

Given the feasible explanations for the observed minor variations in peak positions, heights and breadths between the oxidized glass spectra and the hematite spectrum and the

overall compelling similarity of Raman features between the oxidized glass spectra and the hematite spectrum, the Raman data clearly indicate that hematite is largely responsible for the Fe enrichment observed at the surfaces of the oxidized glasses.

### Interpretation of the Visible and Infrared Spectroscopy Data

The VNIR data can be interpreted in light of the demonstrated presence of hematite in the experimental sample coatings. Both oxidized glass spectra have low reflectivity, which is particularly notable for the  $\text{CO}_2$ -oxidized sample spectrum because it originates from a  $<75\text{ }\mu\text{m}$  particulate sample (Fig. 3) and fine-grained samples tend to yield bright, not dark, spectra. Low reflectivity is consistent with VNIR spectra of gray hematite (e.g., Hunt et al. 1971; Morris et al. 1985; Lane et al. 2002). Both spectra also exhibit an absorption near  $0.47\text{ }\mu\text{m}$ . The position of this feature corresponds to an electronic  $\text{Fe}^{3+}$  transition in hematite (Burns 1993). A distinct absorption at  $0.47\text{ }\mu\text{m}$  is not observed in the VNIR spectrum of pure hematite because the band is typically saturated. The feature does appear in the spectra of samples with minor amounts of hematite dispersed in a scattering matrix (Morris and Lauer 1990). The low reflectivities of the oxidized glass spectra are also consistent with the presence of magnetite in the sample coatings. The VNIR spectrum of magnetite is largely featureless (e.g., Hunt et al. 1971; Morris et al. 1985), making its positive identification in the oxidized glass spectra difficult. Magnetite can exhibit a small reflectivity maximum between  $0.73\text{--}0.81\text{ }\mu\text{m}$  (Morris et al. 1985). However, the position of this maximum falls at longer wavelengths than the reflectivity maxima observed in the coating spectra. The negative spectral slope at wavelengths  $>0.65\text{ }\mu\text{m}$  in the  $\text{CO}_2$ -oxidized spectrum is consistent with the presence of a thin,  $\text{Fe}^{3+}$ -bearing coating over a basalt substrate (Singer and McCord 1979; Fischer and Pieters 1993), though not specifically a hematite coating. The lack of a negative spectral slope across all wavelengths  $>0.74\text{ }\mu\text{m}$  in the air-oxidized sample spectrum may be because the coating is optically thin in the VNIR and/or the coarse particle size of the bulk sample limits scattering.

In the thermal infrared, despite the definitive evidence of hematite in the oxidation-induced coatings, gray hematite-related features like those detected by TES are not apparent in the spectra (Figs. 4 and 7a). The exceptions are the local emissivity maximum at  $497\text{ cm}^{-1}$  and the absorption near  $540\text{ cm}^{-1}$  in the spectrum of the air-oxidized sample (Figs. 4a and 7a). The emissivity maximum falls at effectively the same position as the maximum exhibited by gray hematite near  $500\text{ cm}^{-1}$ . The position of the absorption is consistent with the gray hematite feature near  $560\text{ cm}^{-1}$  (Fig. 7a). Assignment of the  $497\text{ cm}^{-1}$  emissivity maximum and the  $540\text{ cm}^{-1}$  feature to hematite is further supported by

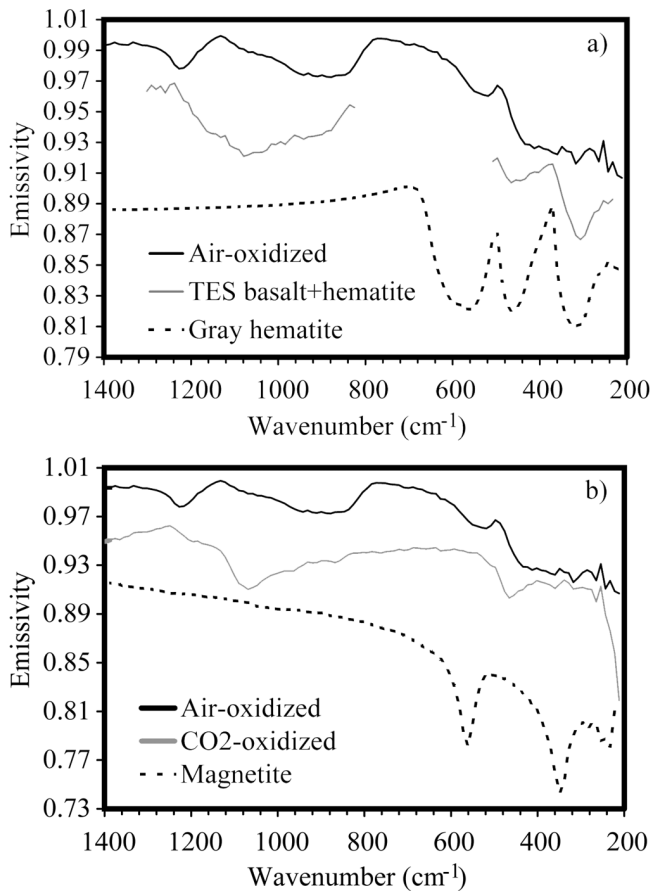


Fig. 7. a) Comparison of hematite signatures in laboratory and natural samples. The black spectrum is the thermal infrared emission spectrum of the air-oxidized sample. The gray spectrum is a TES spectrum from a surface in Meridiani Planum exhibiting both TES basalt and hematite features (Christensen et al. 2001b). Data between 500–800  $\text{cm}^{-1}$  are omitted due to interference from the Martian  $\text{CO}_2$  atmosphere. The dashed spectrum is the thermal infrared emission spectrum of coarse-grained, gray hematite. The depths of the hematite absorption features are scaled for comparison to the other spectra. The TES and hematite spectra are shifted along the emissivity axis for clarity. All spectra have 10  $\text{cm}^{-1}$  spectral resolution; b) comparison of the air-oxidized (black) and  $\text{CO}_2$ -oxidized (gray) sample spectra to the spectrum of magnetite (dashed). The positions of absorptions and emissivity maxima in the magnetite spectrum are not observed in the oxidized glass spectra.

comparison of the air-oxidized sample spectrum to a TES spectrum of a combined basalt and hematite signature (Fig. 7a). Mismatch between the 540  $\text{cm}^{-1}$  band in the air-oxidized spectrum and the 560  $\text{cm}^{-1}$  band in the hematite spectrum, as well as the lack of the 315  $\text{cm}^{-1}$  and well-defined 461  $\text{cm}^{-1}$  gray hematite features in the air-oxidized spectrum possibly result from a number of factors. Hematite stoichiometry, particle size, particle shape, and chemistry can influence band positions and spectral shapes (Estep 1972; Lane et al. 1999; Lane et al. 2002; Glotch et al. 2004) and differences in these factors between coarse-grained, well-crystalline gray hematite and the hematite in the coatings are already suspected in light of the Raman data. The thinness of

the hematite coating might also contribute to the weak expression of hematite features because the coating is optically thin relative to the wavelength of mid-infrared radiation. The even thinner hematite coating on the  $\text{CO}_2$ -oxidized sample coupled with the possible influences of stoichiometry, particle size and chemistry appears to eliminate the signature of the hematite coating in the  $\text{CO}_2$ -oxidized sample spectrum (Figs. 4b and 7a). Hematite features altered or missing to the degree observed in the air- and  $\text{CO}_2$ -oxidized sample spectra are not observed in other studies of various forms of hematite in the thermal infrared (e.g., Estep 1972; Lane et al. 1999, 2002; Glotch et al. 2004; Kirkland et al. 2004). However, these studies did not investigate hematite with the unique form and thickness exhibited by the hematite of this study. Thus, we reasonably conclude that the combination of factors described above is capable of effectively eliminating the 315  $\text{cm}^{-1}$  and 461  $\text{cm}^{-1}$  features of hematite in our data. The lack of hematite-related features between 200–450  $\text{cm}^{-1}$  in both oxidized glass spectra makes it impossible to determine if the hematite in the coatings displays c-axis alignment (i.e., the lack of a 390  $\text{cm}^{-1}$  band), as is observed in the TES-detected gray hematite (Lane et al. 2002). Overall, the expression of hematite in the thermal infrared spectra of the oxidized glasses, while weak, is consistent with the thickness and nature of the hematite.

A number of features in the spectra of the air- and  $\text{CO}_2$ -oxidized samples are not easily attributed to other phases in the samples. These features include the 466  $\text{cm}^{-1}$  feature in the  $\text{CO}_2$ -oxidized spectrum, the feature near 1230  $\text{cm}^{-1}$  in the air-oxidized sample and the overall spectral character of the air- and  $\text{CO}_2$ -oxidized sample spectra between  $\sim 800$ –1100  $\text{cm}^{-1}$ . Possible contributors to the spectra of the oxidized samples are the  $\mu\text{m}$ - to nm-size pyroxene devitrification products, magnetite (as suggested by the Raman data, Fig. 5), bulk oxidized glass, the Ca-rich phase, and, in the air-oxidized samples, pigeonite phenocrysts. Magnetite does not appear to contribute to the oxidized sample spectra in a meaningful way (Fig. 7b). Without work beyond the scope of this study, we cannot isolate the spectral characteristics of the other possible phases in the oxidized samples and, thus, cannot quantitatively determine their contribution to the sample spectra as a whole.

### Hematite Formation Mechanism

A well-understood mechanism exists to explain the formation of hematite on the surface of basalt glass in oxidizing conditions. Cooper et al. (1996) determined that oxidizing conditions induce a coupled migration of divalent cations and charge within an oxidizing glass. The process is initiated by the reaction of  $\text{Fe}^{2+}$  at the glass surface with atmospheric oxygen. Atmospheric oxygen removes electrons from  $\text{Fe}^{2+}$  cations in the glass and the resulting oxygen anions react with either Fe, Ca, or Mg on the glass surface to form oxides. This reaction has three products: the newly created

oxide,  $\text{Fe}^{3+}$  cations in the glass, and a cation vacancy in the glass, created by removal of the cation to form the new oxide. The oxidation process proceeds by migration of  $\text{Fe}^{3+}$  and cation vacancies to the interior of the glass, with the migration of  $\text{Fe}^{3+}$  accommodated by effectively transferring positive charge from an oxidized Fe cation to an unoxidized neighbor in the glass interior ( $\text{Fe}^{3+}$  shifts its positive charge, or a “hole,” to a neighboring  $\text{Fe}^{2+}$ ). As positive charge and cation vacancies migrate inward, mass and charge balance in the glass are maintained by the outward migration of  $\text{Fe}^{2+}$ ,  $\text{Ca}^{2+}$ , or  $\text{Mg}^{2+}$  cations. The divalent cations that reach the surface of the oxidizing glass can then become involved in oxide-producing reactions. As a result, Fe, Ca, and Mg oxides are observed as surficial products of glass oxidation (Cook et al. 1990; Cooper et al. 1996).

The distribution of products resulting from cation migration is dictated by a combination of the mobility and concentration of the cations and the temperature of oxidation. In the experiments of this study, the Fe oxide (hematite) is consistently exterior to the Ca oxide and there is no observed Mg oxide development on the sample surfaces. This distribution requires more efficient Fe migration than Ca migration (and in turn, Mg migration). Experiments of Cooper et al. (1996) and Cook and Cooper (2000) illustrate that at sufficiently high FeO concentrations ( $>1.9$  wt%) and temperatures (700 °C), Fe migration is favored over Ca and Mg migration. The temperature of the experiments in this study (700 and 900 °C) are high enough to favor Fe migration and the FeO concentration of the basalt glasses ( $\sim 19.5$  wt%), a result of their Martian meteorite-like nature, is well above the minimum FeO concentration. FeO is also present in much greater concentration than either CaO ( $\sim 9$  wt%) or MgO (5–7 wt%) in the glasses, further favoring its migration during oxidation relative to the other two cations. The higher concentration of CaO relative to MgO in the glasses is consistent with the presence of a Ca-enriched layer and the absence of an Mg-enriched layer near the surface of the oxidized glasses. The behaviors of divalent cations in response to temperature and concentration support the observed distribution of Fe, Ca, and Mg at the surfaces of the oxidized glasses. The high temperatures of the experiments and the high concentration of Fe combine to facilitate hematite formation on the surfaces of the oxidized glasses.

The lack of chemical gradient development observed in the product of the 350 °C experiment (Fig. 1e) suggests that high oxidation temperatures are necessary to induce cation migration and, ultimately, hematite coating formation. Thus, hematite coating formation is not expected on already emplaced glass-rich basalt flows exposed to moderately elevated temperature environments such as reheating during nearby magma emplacement or nearby hydrothermal activity. Rather, the high temperatures necessary to induce hematite coating formation are expected to exist only during initial extrusion of glass-rich basalt flows.

### Terrestrial Analog for Process

While laboratory studies provide a formation mechanism for hematite coatings on basalt glasses and suggest that such coatings would form during basalt extrusion, is it possible for the process to act in geologically relevant conditions? We studied the gray, metallic sheen commonly observed on newly extruded Hawaiian basalt flows as an apparent analogue to the hematite coatings on the experimental basalts. Our Hawaiian basalt was collected from cooling pahoehoe films in October 2001 (K. Hibbits, personal communication) and we subjected it to the same suite of SEM and Raman analyses used to study the experimentally oxidized basalts. Elemental maps of the metallic sheen on the Hawaiian basalt indicate that the sheen corresponds to Fe- and Ca-rich layers in the same geometry as those observed on the experimentally oxidized basalts (Fig. 1f). The Fe- and Ca-rich layers range in thickness from 0.5–0.7  $\mu\text{m}$ . The presence of the Fe- and Ca-enriched layers at the surface of a naturally emplaced glass-rich basalt suggests that the process active in the experimentally oxidized basalts is also active in naturally oxidized basalts.

Raman analyses further indicate that the experimentally oxidized samples capture a natural hematite formation process. Initial Raman analysis of the surface of the Hawaiian basalt led to alteration of the gray, metallic sheen under the laser as evidenced by fluorescence and nearly featureless Raman spectra. Substituting a 20 $\times$  objective for the 50 $\times$  objective expanded the area over which the laser power was distributed and eliminated the occurrence of alteration. The resulting Raman spectrum of the Hawaiian sheen exhibits peaks near 216, 285, and 400  $\text{cm}^{-1}$  and broad peaks near 650 and 1300  $\text{cm}^{-1}$  which correspond to the positions of Raman peaks exhibited by hematite (Fig. 8) and the experimentally oxidized basalt glasses (Fig. 5). A portion of the peaks in the Raman spectrum of the unoxidized glassy bottom of the Hawaiian sample (Fig. 2c) occur at positions similar to those of peaks in the Raman spectrum of the sheen. However, we favor assignment of peaks exhibited by the sheen to hematite primarily because the broad peak near 1300  $\text{cm}^{-1}$  corresponds to a peak resulting from the antiferromagnetic nature of hematite (de Faria et al. 1997), which makes the peak diagnostic of hematite. Confirmation that the Fe enrichment at the surface of the Hawaiian basalt is hematite fully demonstrates that the oxidation experiments reproduce a naturally occurring process and supports the deduction that hematite coatings can form on the surfaces of glassy basalts during extrusion. The Hawaiian basalt also demonstrates that high, Martian meteorite-like concentrations of FeO in a basalt glass are not required for hematite formation.

### CONCLUSIONS AND IMPLICATIONS

Glass-rich basalts with Martian meteorite-based chemistry (high FeO, low  $\text{Al}_2\text{O}_3$ ) oxidized at high (700 and

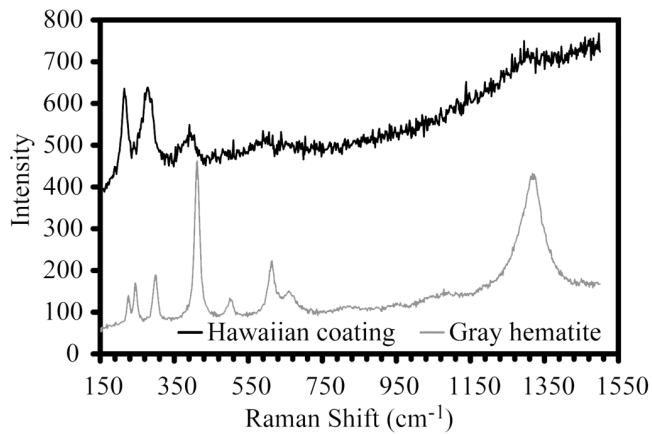


Fig. 8. Raman spectra from the surface of a Hawaiian basalt with a gray, metallic coating (black) and a pure, coarse-grained gray hematite sample (gray). The similarities between the spectra suggest that the sheen, and corresponding Fe enrichment (Fig. 1f), results from the presence of hematite. Both spectra were excited using a 514.5 nm Ar laser.

900 °C) temperatures in air and CO<sub>2</sub>, respectively, form thin (<1 μm) hematite coatings on the outermost surfaces of the glasses. Hematite is manifested macroscopically by development of magnetism and a gray, metallic sheen on the glass surface and microscopically by Fe enrichment at the glass surface observed in element maps. Raman analyses confirm that the Fe enrichment at the surfaces of the oxidized glasses corresponds to hematite, and some possible magnetite, mineralization. Glass-rich basalt oxidized at lower temperatures (350 °C) does not develop any evidence of hematite formation. Thus, hematite formation is concluded to occur only at high temperatures, likely during extrusion and emplacement of glass-rich basalt. Hematite formation on basaltic glass is enabled by an oxidation mechanism that induces migration of divalent cations, most notably Fe<sup>2+</sup>, to the surface of an oxidizing glass (e.g., Cooper et al. 1996). Once concentrated at the surface of an oxidizing basalt glass, the Fe<sup>2+</sup> cations can be oxidized and form hematite. A terrestrial “proof of concept” is provided by Hawaiian basalt with a gray, metallic sheen that corresponds to a thin hematite coating. Hematite coating development on a Hawaiian basalt with 10–11 wt% FeO demonstrates that Martian meteorite-like FeO contents (~19 wt% FeO; Minitti and Rutherford 2000) are not required for a basalt glass to form a hematite coating and that such coatings indeed form during extrusion.

The experimentally oxidized basalt glasses and the Hawaiian basalt analogue strongly suggest that hematite can form on Martian basalts during extrusion whether they are like those observed by TES or like Martian meteorite basalts. Concentrations of FeO extrapolated from mineralogies of the TES basalt determined through linear deconvolution of the TES surface type 1 spectrum (Christensen et al. 2000a; Bandfield et al. 2000) range between 5–15 wt% FeO (McSween et al. 2003). This range of TES basalt FeO

contents overlaps the FeO content of the Hawaiian basalt of this study suggesting that TES basalt contains adequate amounts of FeO for hematite coating formation. Concentrations of FeO in rocks measured on the Martian surface by Mars Pathfinder (e.g., Foley et al. 2003) and MER (Gellert et al. 2004) are also sufficient to have facilitated hematite coating formation, if those rocks or their counterparts at the respective landing sites were glass-bearing igneous rocks.

If hematite coatings formed by oxidation during basalt extrusion are present on the Martian surface, their detectability by Mars remote sensing instruments varies with wavelength. In the VNIR, the spectral range and resolution capabilities of current (OMEGA; Bibring et al. 2004) and future (CRISM; Murchie et al. 2002) instruments are sufficient to distinguish differences between the spectra of hematite-coated glassy basalts and their unoxidized counterparts (Fig. 3). Further, the distinction could be observed from either coarse or fine particle size materials (Fig. 3). However, the relatively subtle features associated with the hematite coating (low reflectivity, absorption near 0.47 μm, negative spectral slope across a portion of wavelengths >0.74 μm) could also be assigned to other Fe<sup>3+</sup>-bearing materials, making unique detection of hematite-coated basalts like those of this study difficult. Recognition of hematite-coated basalts could also be hindered by the presence of bright dust (Morris et al. 1989). If VNIR spectra like those of the oxidized samples in Fig. 3 were obtained from Mars, imaging data that reveal the geologic context of the source of the spectra and/or albedo data might enable positive identification of hematite coated basalts. In the thermal infrared, the oxidized sample spectra (Fig. 4) have the same spectral range and resolution as TES data, illustrating that detection of hematite coatings is possible with TES. The coating crystallinity and thickness and corresponding subtlety (or lack) of features in the thermal infrared, however, makes hematite coating detection even more challenging than in the VNIR. The oxidized spectra suggest that a hematite coating must have a minimum thickness of ~1 μm to yield features diagnostic of hematite in the thermal infrared (Fig. 4a). Because the combined Raman and thermal infrared data of this study suggest that hematite crystallinity and particle size influence the strength of the hematite signature in the thermal infrared, thinner coatings might require some form of metamorphism to coarsen and/or recrystallize the hematite in the coatings to enable detection.

Despite challenges associated with its unique detection, hematite originating from oxidation of glassy basalt flows is potentially abundant on Mars given the widespread occurrence of volcanic materials on the Martian surface (Mouginis-Mark et al. 1992; Bandfield et al. 2000). Hematite coatings formed on oxidized, glassy basalt flows easily could be physically weathered off and contribute to the red hematite observed in the Martian soil. Hematite

coatings like those in this study do not yield a thermal infrared signature like that of the gray hematite detected by TES. Additionally, the recent apparent evidence for the role of water in the formation of hematite and its associated deposits at the Meridiani landing site (e.g., Christensen et al. 2004; Herkenhoff et al. 2004) seems to discount the possibility that the Meridiani hematite represents a hematite coating produced during extrusion of a glassy basalt flow. Given similar, water-related sedimentary origins proposed for the hematite-associated materials in Aram Chaos and Valles Marineris (Nedell et al. 1987; Christensen et al. 2001b; Glotch and Christensen 2003; Weitz et al. 2003), it may also be unlikely that hematite-coated basalts like those in this study are the source of the hematite signature in these regions. However, formation of the gray hematite in Aram Chaos and Valles Marineris by glassy basalt flow oxidation during extrusion should not be discounted as these sites are studied further. If gray hematite originating as coatings on glassy basalt flows is an important source of Martian hematite, as may well have been the case in other areas of Mars, it removes the requirement of water as an initial alteration agent of Martian crustal materials. The new hematite formation mechanism presented here should be taken into consideration when assessing the nature and source of the hematite component of Martian surface materials and the role of water as a necessary agent in hematite formation.

*Acknowledgments*—M. E. Minitti would like to thank numerous parties for their assistance with this work. Jack Mustard of Brown University drove the discovery of the gray hematite coatings on the original experimental samples. Karl Hibbitts of Planetary Science Institute kindly provided Hawaiian basalts ideal for this study. George Wolf in the Department of Chemistry at Arizona State University provided early guidance and analyses in his Raman spectroscopy laboratory. George Rossman in the Division of Geological and Planetary Sciences at Caltech graciously opened his lab for analysis of the samples and Elizabeth Miura provided expert analytical and proof-reading capabilities. The authors wish to thank Neena Rodricks, Vicky Hamilton, and Allan Treiman for reviews that clarified the paper. RELAB is a multi-user facility at Brown University supported by NASA grant NAG5-3871. A portion of this work was funded through the NASA Mars Global Surveyor Data Analysis Program (MDL) and Mars Data Analysis and Mars Fundamental Research programs (JLB).

*Editorial Handling*—Dr. Allan Treiman

## REFERENCES

- Bandfield J. L., Hamilton V. E., and Christensen P. R. 2000. A global view of Martian surface compositions from MGS-TES. *Science* 287:1626–1630.
- Bell J. F., III, McCord T. B., and Owensby P. D. 1990. Observational evidence of crystalline iron oxides on Mars. *Journal of Geophysical Research* 95:14,447–14,461.
- Bibring J. P., Langevin Y., Poulet F., Gendrin A., Gondet B., Berthé M., Soufflot A., Drossart P., Combes M., Bellucci G., Moroz V., Mangold N., Schmitt B., and the OMEGA team. 2004. Perennial water ice identified in the south polar cap of Mars. *Nature* 428: 627–630.
- Bishop J. L., Fröschl H., and Mancinelli R. L. 1998. Alteration processes in volcanic soils and identification of exobiologically important weathering products on Mars using remote sensing. *Journal of Geophysical Research* 103:31,457–31,476.
- Bishop J. L., Schiffman P., and Southard R. J. 2002. Geochemical and mineralogical analyses of palagonitic tuffs and altered rinds of pillow lavas on Iceland and applications to Mars. In *Volcano-ice interactions on Earth and Mars*, edited by Smellie J. L. and Chapman M. G. Special Publication No. 202. London: The Geological Society. pp. 371–392.
- Bishop J. L., Schiffman P., Southard R. J., Drief A., Verosub K. L., and Smith D. J. 2004. Classifying terrestrial volcanic alteration processes and defining alteration processes they represent on Mars (abstract #1780). 35th Lunar Planetary Science Conference. CD-ROM.
- Burns R. G. 1993. Origin of electronic spectra of minerals in the visible to near-infrared region. In *Remote geochemical analysis: Elemental and mineralogical composition*, edited by Pieters C. M. and Englert P. A. J. New York: Cambridge University Press. pp. 3–29.
- Christensen P. R., Anderson D. L., Chase S. C., Clark R. N., Kieffer H. H., Malin M. C., Pearl J. C., Carpenter J., Bandiera N., Brown F. G., and Silverman S. 1992. Thermal emission spectrometer experiment; Mars Observer mission. *Journal of Geophysical Research* 97:7719–7734.
- Christensen P. R., Bandfield J. L., Smith M. D., Hamilton V. E., and Clark R. N. 2000a. Identification of a basaltic component on the Martian surface from the Thermal Emission Spectrometer data. *Journal of Geophysical Research* 105:9609–9621.
- Christensen P. R., Bandfield J. L., Clark R. N., Edgett K. S., Hamilton V. E., Hoefen T., Kieffer H. H., Kuzmin R. O., Lane M. D., Malin M. C., Morris R. V., Pearl J. C., Pearson R., Roush T. L., Ruff S. W., and Smith M. D. 2000b. Detection of crystalline hematite mineralization on Mars by the Thermal Emission Spectrometer: evidence for near-surface water. *Journal of Geophysical Research* 105:9623–9642.
- Christensen P. R., Bandfield J. L., Hamilton V. E., Ruff S. W., Kieffer H. H., Titus T. N., Malin M. C., Morris R. V., Lane M. D., Clark R. L., Jakosky B. M., Mellon M. T., Pearl J. C., Conrath B. J., Smith M. D., Clancy R. T., Kuzmin R. O., Roush T., Mehall G. L., Gorelick N., Bender K., Murray K., Dason S., Greene E., Silverman S., and Greenfield M. 2001a. Mars Global Surveyor Thermal Emission Spectrometer experiment: Investigation description and surface science results. *Journal of Geophysical Research* 106:23,823–23,871.
- Christensen P. R., Morris R. V., Lane M. D., Bandfield J. L., and Malin M. C. 2001b. Global mapping of Martian hematite mineral deposits: Remnants of water-driven processes on early Mars. *Journal of Geophysical Research* 106:23,873–23,886.
- Christensen P. R., Wyatt M. B., Glotch T. D., Rogers A. D., Anwar S., Arvidson R. E., Bandfield J. L., Blaney D. L., Budney C., Calvin W. M., Fallacaro A., Fergason R. L., Gorelick N., Graff T. G., Hamilton V. E., Hayes A. G., Johnson J. R., Knudson A. T., McSween H. Y., Jr., Mehall G. L., Mehall L. K., Moersch J. E., Morris R. V., Smith M. D., Squyres S. W., Ruff S. W., and Wolff M. J. 2004. Mineral compositions and abundances at the Meridiani Planum site from the Mini-TES experiment on the Opportunity rover. *Science* 306:1733–1739.

- Cook G. B. and Cooper R. F. 2000. Iron concentration and the physical processes of dynamic oxidation in an alkaline earth aluminosilicate glass. *American Mineralogist* 85:397–406.
- Cook G. B., Cooper R. F., and Wu T. 1990. Chemical diffusion and crystalline nucleation during oxidation of ferrous iron-bearing magnesium aluminosilicate glass. *Journal of Non-Crystalline Solids* 120:207–222.
- Cooper R. F., Fanselow J. B., and Poker D. B. 1996. The mechanism of oxidation of a basaltic glass: Chemical diffusion of network-modifying cations. *Geochimica et Cosmochimica Acta* 60:3253–3265.
- de Faria D. L. A., Silva S. V., and de Oliveira M. T. 1997. Raman microscopy of some iron oxides and oxyhydroxides. *Journal of Raman Spectroscopy* 28:873–878.
- Deines P., Nafziger R. A., Ulmer G. C., and Woerman E. 1974. Temperature-oxygen fugacity tables for selected gas mixtures in the system C-H-O at one atmosphere total pressure. *Bulletin of the Earth and Mineral Sciences Experiment Station* 88. pp. XX–XX.
- Estep P. A. 1972. Infrared spectroscopic studies of hematite. M.S. thesis, West Virginia University, Morgantown, West Virginia, USA.
- Fischer E. and Pieters C. M. 1993. The continuum slope of Mars: Bidirectional reflectance investigations and applications to Olympus Mons. *Icarus* 102:185–202.
- Gellert R., Rieder R., Anderson R. C., Bruckner J., Clark B. C., Dreibus G., Economou T., Klingelhofer G., Lugmair G. W., Ming D. W., Squyres S. W., d'Uston C., Wanke H., Yen A., and Zipfel J. 2004. Chemistry of rocks and soils in Gusev Crater from the alpha particle X-ray spectrometer. *Science* 305:829–832.
- Glotch T. D. and Christensen P. R. 2003. The geology of Aram Chaos (abstract #2046). 34th Lunar Planetary Science Conference. CD-ROM.
- Glotch T. D., Morris R. V., Christensen P. R., and Sharp T. G. 2004. Effect of precursor mineralogy on the thermal infrared emission spectra of hematite: Application to Martian hematite mineralization. *Journal of Geophysical Research* 109, doi: 10.1029/2003JE002224.
- Herkenhoff K. E., Squyres S. W., Arvidson R., Bass D. S., Bell J. F., III, Bertelsen P., Ehlmann B. L., Farrand W., Gaddis L., Greeley R., Grotzinger J., Hayes A. G., Hviid S. F., Johnson J. R., Jolliff B., Kinch K. M., Knoll A. H., Madsen M. B., Maki J. N., McLennan S. M., McSween H. Y., Ming D. W., Rice J. W., Jr., Richter L., Sims M., Smith P. H., Soderblom L. A., Spanovich N., Sullivan R., Thompson S., Wdowiak T., Weitz C., and Whelley P. 2004. Evidence from Opportunity's Microscopic Imager for water on Meridiani Planum. *Science* 306:1727–1730.
- Hunt G. R., Salisbury J. W., and Lenhoff C. J. 1971. Visible and near-infrared spectra of minerals and rocks: III. Oxides and hydroxides. *Modern Geology* 2:195–205.
- Kirkland L. E., Herr K. C., and Adams P. M. 2004. A different perspective for the Mars rover Opportunity site: Fine-grained, consolidated hematite and hematite coatings. *Geophysical Research Letters* 31, doi:10.1029/2003GL019284.
- Lane M. D., Morris R. V., and Christensen P. R. 1999. Spectral behavior of hematite at visible/near infrared and midinfrared wavelengths (abstract #6085). 5th International Conference on Mars. CD-ROM.
- Lane M. D., Morris R. V., Mertzman S. A., and Christensen P. R. 2002. Evidence for platy hematite grains in Sinus Meridiani, Mars. *Journal of Geophysical Research* 107, doi:10.1029/2001JE001832.
- McMillan P. F. and Hofmeister A. M. 1988. Infrared and Raman spectroscopy. In *Spectroscopic methods in mineralogy and geology*, edited by Hawthorne F. C. Washington D.C.: Mineralogical Society of America. pp. 99–159.
- McSween H. Y., Jr., Grove T. L., and Wyatt M. B. 2003. Constraints on the composition and petrogenesis of the Martian crust. *Journal of Geophysical Research* 108, doi:10.1029/2003JE002175.
- Minitti M. E. and Rutherford M. J. 2000. Genesis of the Mars Pathfinder "sulfur-free" rock from SNC parental liquids. *Geochimica et Cosmochimica Acta* 64:2535–2547.
- Minitti M. E., Mustard J. F., and Rutherford M. J. 2002. Effects of glass content and oxidation on the spectra of SNC-like basalts: Applications to Mars remote sensing. *Journal of Geophysical Research* 107, doi:10.1029/2001JE001518.
- Morris R. V. and Lauer H. V., Jr. 1990. Matrix effects for reflectivity spectra of dispersed nanophase (superparamagnetic) hematite with application to Martian spectral data. *Journal of Geophysical Research* 95:5101–5109.
- Morris R. V., Lauer H. V., Jr., Lawson C. A., Gibson E. K., Jr., Nace G. A., and Stewart C. 1985. Spectral and other physicochemical properties of submicron powders of hematite ( $\alpha$ -Fe<sub>2</sub>O<sub>3</sub>), maghemite ( $\gamma$ -Fe<sub>2</sub>O<sub>3</sub>), magnetite (Fe<sub>3</sub>O<sub>4</sub>), goethite ( $\alpha$ -FeOOH), and lepidocrocite ( $\gamma$ -FeOOH). *Journal of Geophysical Research* 90:3126–3144.
- Morris R. V., Agresti D. G., Lauer H. V., Jr., Newcomb J. A., Shelfer T. D., and Murali A. V. 1989. Evidence for pigmentary hematite on Mars based on optical, magnetic, and Mössbauer studies of superparamagnetic (nanocrystalline) hematite. *Journal of Geophysical Research* 94:2760–2778.
- Morris R. V., Gooding J. L., Lauer H. V., Jr., and Singer R. B. 1990. Origins of Mars-like spectral and magnetic properties of a Hawaiian palagonitic soil. *Journal of Geophysical Research* 95: 14,427–14,434.
- Morris R. V., Golden D. C., Bell J. F., III, Lauer H. V., Jr., and Adams J. B. 1993. Pigmenting agents in Martian soils: Inferences from spectral, Mössbauer, and magnetic properties of nanophase and other iron oxides in Hawaiian palagonitic soil PN-9. *Geochimica et Cosmochimica Acta* 57:4597–4609.
- Morris R. V., Shelfer T. D., Scheinost A. C., Hinman N. W., Furniss G., Mertzman S. A., Bishop J. L., Ming D. W., Allen C. C., and Britt D. T. 2000. Mineralogy, composition, and alteration of Mars Pathfinder rocks and soils: Evidence from multispectral, elemental, and magnetic data on terrestrial analogue, SNC meteorite, and Mars Pathfinder samples. *Journal of Geophysical Research* 105:1757–1817.
- Mouginis-Mark P. J., Wilson L., and Zuber M. T. 1992. The physical volcanology of Mars. In *Mars*, edited by Kieffer H. H., Jakosky B. M., Snyder C. W., and Matthews M. S. Tucson: The University of Arizona Press. pp. 424–452.
- Murchie S., Arvidson R., Barnouin-Jha O., Beisser K., Bibring J. P., Bishop J., Boldt J., Choo T., Clancy R. T., Darlington E. H., Des Marais D., Fort D., Hayes J., Lees J., Malaret E., Mehoke D., Morris R., Mustard J., Peacock K., Robinson M., Roush T., Schaefer E., Silverglate P., Smith M., Thompson P., and Tossman B. 2002. CRISM: Compact Reconnaissance Imaging Spectrometer for Mars on the Mars Reconnaissance Orbiter (abstract #1697). 33rd Lunar Planetary Science Conference. CD-ROM.
- Nedell S. S., Squyres S. W., and Anderson D. W. 1987. Origin and evolution of the layered deposits in the Valles Marineris, Mars. *Icarus* 70:409–441.
- Schiffman P., Southard R. J., Eberl D. D., and Bishop J. L. 2002. Distinguishing palagonitized from pedogenically-altered basaltic Hawaiian tephra: Mineralogical and geochemical criteria. In *Volcano-ice interactions on Earth and Mars*, edited by Smellie J. L., and Chapman M. G. Special Publication No. 202. London: The Geological Society. pp. 393–405.

- Schiffman P., Spero H. J., Southard R. J., and Swanson D. A. 2000. Controls on palagonitization versus pedogenic weathering of basaltic tephra: Evidence from the consolidation and geochemistry of the Keanakako'i ash member, Kilauea volcano. *Geochemistry, Geophysics, Geosystems* 1, doi:10.1029/2000GC000068.
- Shebanova O. N. and Lazor P. 2003. Raman study of magnetite ( $\text{Fe}_3\text{O}_4$ ): Laser-induced thermal effects and oxidation. *Journal of Raman Spectroscopy* 34:845–852.
- Simon I. and McMahon H. O. 1953. Study of some binary silicate glasses by means of reflection in the infrared. *Journal of the American Ceramic Society* 36:160–164.
- Singer R. B. and McCord T. B. 1979. Mars: Large scale mixing of bright and dark surface materials and implications for analysis of spectral reflectance. Proceedings, 10th Lunar and Planetary Science Conference. pp. 1835–1848.
- Tuinstra F. and Koenig J. L. 1970. Raman spectrum of graphite. *Journal of Chemical Physics* 53:1126–1130.
- Wang A., Haskin L. A., and Jolliff B. L. 1998. Characterization of mineral products of oxidation and hydration by laser Raman spectroscopy: Implications for in situ petrologic investigation on the surface of Mars (abstract #1819). 28th Lunar Planetary Science Conference. CD-ROM.
- Weitz C. M., Parker T. J., Bulmer M., Anderson F. S., and Grant J. A. 2003. Geology of the Melas Chasma landing site for MER. *Journal of Geophysical Research* 108, doi:10.1029/2002JE002022.
-